PAPER

Check for updates

RSM-BBD optimization of room-temperature synthesized ZIF-8 for synergistic adsorption-photocatalysis of RhB

Sanaa Essalmi, [ab] Véronique Madigou, [b] Amane Jada, [cd] Amal BaQais, [e] Mohamed Saadi, [a] Hassan Ait Ahsaine [*a] and Madjid Arab [*b]

Three ZIF-8 nanomaterials with different Zn : 2-methylimidazole molar ratios (1 : 30, 1 : 50, and 1 : 70) were synthesized at room temperature in aqueous medium within 30 minutes without surfactants. Structural analyses confirmed the formation of mesoporous ZIF-8 with distinct morphologies, ranging from spherical assemblies to rhombic dodecahedra. Response Surface Methodology using a Box–Behnken design (RSM-BBD) was applied to optimize five parameters (pH, contact time, pollutant dose, linker amount, and catalyst weight) governing rhodamine B (RhB) removal. Under optimized conditions (pH 7, 70 mg catalyst, 10 ppm RhB, 60 min contact), ZIF-8 with a 1 : 70 ratio achieved a maximum adsorption capacity of 91.7 mg g^{-1} and a removal efficiency of ~91%, fitting well with the Langmuir model (R^2 = 0.97). Photodegradation studies revealed high activity under UV irradiation, with rate constants of 0.00812, 0.00215, and 0.0014 min^{-1} for ZIF-8 (1 : 30, 1 : 50, and 1 : 70), respectively. The materials also demonstrated excellent recyclability, retaining over 92% efficiency after five cycles. The novelty of this work lies in the systematic evaluation of the Zn : 2-Hmim molar ratio on the morphology and performance of ZIF-8, combined with the first application of RSM-BBD to optimize the dual adsorption–photodegradation process for RhB removal. These findings provide new insights into tailoring ZIF-8 synthesis for efficient wastewater treatment applications.

1. Introduction

The widespread industrial utilization of organic dyes in various sectors, including textiles, paints, paper, and plastics, has resulted in significant environmental contamination. The release of dye-laden wastewater into aquatic ecosystems poses a severe threat to both ecological health and human well-being.[1] Consequently, there is an urgent need for more sustainable and efficient approaches to remove organic dyes from wastewater.[2,3]

Metal–organic frameworks (MOFs) are crystalline materials composed of metal ions or clusters that are linked together by organic molecules, forming a three-dimensional network with numerous pores. Their extensive surface area, adaptable structure, and resistance to degradation make them well-suited for applications in water treatment and purification.[4–11] Numerous studies have demonstrated the effectiveness of MOFs, such as HKUST-1, UiO-66,Fe-MOF, ZIF-8, and ZIF-67, in removing a wide range of contaminants from water, including heavy metals such as chromium and mercury,[12] and organic molecules like methylene blue and rhodamine B.[13] The adsorption mechanisms involved in these processes typically involve electrostatic interactions, hydrogen bonding, and π–π stacking between the dye molecules and the MOF surface.[14–20]

Among the various MOFs, zeolitic imidazolate framework-8 (ZIF-8) has garnered significant attention due to its exceptional performance in organic dye removal. ZIF-8 is a crystalline material formed by connecting zinc ions in a tetrahedral arrangement with 2-methylimidazole linkers, resulting in a structure like mineral sodalite. This structure provides a high specific surface area and porosity, making ZIF-8 an attractive material for a wide range of applications, including gas storage, catalysis, and membrane fabrication.[21–26] In addition to its excellent adsorption properties, ZIF-8 exhibits several other desirable characteristics. It is chemically inert in aqueous solutions, ensuring its stability under a wide range of environmental conditions. Moreover, the size of ZIF-8 crystals can be tailored from the nanoscale to the microscale, allowing for the optimization of its adsorption capacity and selectivity. ZIF-8 is advantageous as it is bifunctional: materials can adsorb and degrade organic pollutants under the effect of light in specific

a Laboratoire de Chimie Appliquée des Matériaux, Faculté des Sciences, Mohammed V University in Rabat, Morocco. E-mail: h.aitahsaine@um5r.ac.ma; madjid.arab@univ-tln.fr

b Université de Toulon, AMU, CNRS, IM2NP, CS 60584, Toulon Cedex 9, France

c Université de Haute-Alsace, Institute des Matériaux de Mulhouse (IS2M)-CNRS UMR 7361, Mulhouse, France

d Université de Strasbourg, Strasbourg, France

e Department of Chemistry, College, of Science, Princess Nourah Bint Abdulrahman University, P. O. Box 84428, Riyadh 11671, Saudi Arabia

conditions.[7,27–32] Experimental studies have revealed that the surface of ZIF-8 is enriched with zinc ions and terminated with multiple functional groups, including hydroxide, carbonates, and amines, in addition to methylimidazole groups. These functional groups play a crucial role in the adsorption of organic dyes by providing sites for electrostatic interactions, hydrogen bonding, and other binding mechanisms.[33–38]

The effectiveness of contaminant removal through adsorption–photodegradation onto materials is influenced by various factors, including the initial concentration of the pollutants, material dosage, contact time, solution pH, and more. To evaluate the combined impact of these variables on adsorption efficiency, optimization techniques are often employed. Response Surface Methodology (RSM) has emerged as a powerful tool for such studies. Compared to traditional univariate analysis, RSM offers advantages in terms of minimizing the number of experimental runs required, thereby reducing costs and time. Additionally, it effectively illustrates the interplay between influential factors.[39–54] To our knowledge, the optimization of adsorption–degradation processes for organic dyes, such as rhodamine B (RhB), using ZIF-8 as an adsorbent and RSM as a statistical analysis tool has not been previously explored, particularly considering the significance of the molar ratio in the ZIF-8 synthesis process.

Despite extensive research into using ZIF-8 for organic dye removal, there remains a lack of comprehensive studies investigating how the molar ratio of metal to organic linker directly influences its adsorption and photodegradation performance. This parameter is likely to significantly impact the structural properties, surface chemistry, and adsorption capacity of ZIF-8. By systematically exploring the effects of the molar ratio, it may be possible to optimize the synthesis of ZIF-8 to achieve even higher levels of dye removal efficiency. Especially since we are moving from a rare morphology to a completely different one, which is the most commonly reported one in literature.[55–58]

In this study, the ZIF-8 crystals from $Zn(NO_3)_2 \cdot 6H_2O$ and 2-HmiM linker were rapidly synthesized under stirring for 30 min at room temperature. Three products, with different molar ratio between Zn^{2+} and 2-HMim 1 : 30, 1 : 50, and 1 : 70 obtained. The products were characterized using various techniques such as X-ray diffraction (XRD), Fourier-transform infrared spectroscopy (FTIR), transmission electron microscopy (TEM) and nitrogen sorption studies (BET). A response surface methodology approach was adopted to optimize the experimental parameters for the removal of RhB. The influence of molar ratio, solution concentration, pH, contact duration, and ZIF-8 dosage on adsorption performance was thoroughly examined. In addition, possible adsorption pathways were outlined, emphasizing the significance of electrostatic forces and π–π interactions. In addition, the photodegradation of the pollutant was studied for the three materials.

2 Experimental section

2.1. Materials and reagents

All chemicals involving rhodamine B (RhB), 2-methylimidazole (2-HMim), zinc(ɪɪ) nitrate hexahydrate [Zn (NO₃)₂·6H₂O],

ethanol (C_2H_5OH), disodium tetra-acetate (EDTA, 99.8%), ʟ-ascorbic acid (99.9%), isopropanol (IPA, 99,9%) were commercially purchased from SigmaAldrich and were used without further purification.

2.2. Synthesis of ZIF-8 materials

Three ZIF-8 nanocrystals were synthesized by a direct precipitation procedure with modifications.[58] In a typical procedure, 1.0 mmol of $Zn(NO_3)_2 \cdot 6H_2O$ (0.297 g) was dissolved in deionized water to form a clear solution. Separately, the organic linker 2-methylimidazole was dissolved in deionized water in three different amounts corresponding to the targeted molar ratios of Zn^{2+} : 2-Hmim of 1 : 30, 1 : 50, and 1 : 70. Accordingly, 30 mmol (2.46 g), 50 mmol (4.11 g), and 70 mmol (5.75 g) of 2-Hmim were used for the synthesis of ZIF-8.30, ZIF-8.50, and ZIF-8.70, respectively. The linker solution was rapidly poured into the zinc solution under vigorous stirring, and the mixture was maintained under continuous stirring at room temperature for 30 min, during which a white suspension appeared. The precipitated products were collected by centrifugation and washed three times with deionized water to remove unreacted species. They were then dried at 60 °C for 18 h in an air-flow oven to yield the final ZIF-8.30, ZIF-8.50, and ZIF-8.70 powders.

The synthesis route adopted here is simple, fast and environmentally friendly, allowing reproducible preparation of ZIF-8 materials under mild conditions. Its limitation, however, lies in the reduced control of morphology at lower Zn : 2-Hmim ratios, which may influence subsequent performance.

2.3. Material characterizations

The structural features of ZIF-8 powders were analyzed using X-ray diffraction (XRD) on a Rigaku diffractometer equipped with a Cu Kα radiation source ($\lambda = 1.5440$ Å) and a Ni filter to suppress Kβ emission. Measurements were conducted over a 2θ range of 5–60° with an incremental step of 0.02°. In addition, Fourier-transform infrared (FTIR) spectroscopy was employed to investigate the vibrational modes of the synthesized material, with spectra recorded at room temperature using a dedicated spectrometer. The ZIF-8 crystals morphologies were examined by scanning electron microscopy (SEM) (Supra 40 VP Gemini Zeiss operated at 5 kV) and transmission electron microscopy (TEM, Tecnai G2 200 kV). In addition, the N_2 adsorption/desorption isothermal measurements were recorded at 77 K on the Quatachroms instrument (AutosorbiQ, USA) to determine textural properties. X-ray photoelectron spectroscopy (XPS) analyses were carried out using Scienta SES-2002 in Mulhouse, France. The optical absorption range and bandgap energy of ZIF-8 were determined by recording the absorption spectra within 200–800 nm using a Shimadzu UV-1800 UV-visible spectrophotometer. To further elucidate the photocatalytic behavior, the conduction band (CB) and valence band (VB) edge positions of ZIF-8 were estimated through Mott–Schottky analysis (OrigaLys electrochemical workstation) at 300 Hz in which E_{CB} is the conduction band edge, E_{VB} is the valence band as follows:[59,60]

$$E_{fb} \text{ (V } vs. \text{ NHE)} = 0.197 \ (E°(\text{Ag/AgCl})) + 0.059\text{pH}$$
$$+ \ E_{fb} \text{ (V } vs. \text{ Ag/AgCl)} \tag{1}$$

$$E_{CB} = E_{fb} - 0.2 \tag{2}$$

$$E_{VB} = Eg + E_{CB} \tag{3}$$

Photoluminescence (PL) spectra and time-resolved fluorescence (TRFL) decay profiles were recorded using a Horiba Fluoromax fluorescence spectrophotometer. The decay behavior was analyzed through a bi-exponential fitting approach, as expressed in eqn (4):

$$I_t = I_1 \ e^{-(t/\tau 1)} + I_2 \ e^{-(t/\tau 2)} \tag{4}$$

Here, I_1 and I_2 represent the respective emission intensities, while τ_1 and τ_2 denote their associated lifetimes. The mean fluorescence lifetime was calculated according to eqn (5): s

$$\tau_{moy} = \frac{I_1\tau_1^2 + I_2\tau_2^2}{I_1\tau_1 + I_2\tau_2} \tag{5}$$

2.4. BBD-RSM design and data analysis

To optimize the experimental parameters, a Box–Behnken design (BBD) based on response surface methodology (RSM) was employed. This approach allowed the evaluation of the combined effects of pollutant dose, linker amount, pH, contact time, and catalyst weight on RhB removal efficiency (Table S1). Comprehensive details of the design, factor levels, regression models, and statistical validation are presented in the SI.

3 Results and discussion

3.1. Structural analysis

Fig. 1 illustrates the XRD patterns of the as-prepared ZIF-8 materials. The observed diffraction peaks at 2θ values of 7.28°, 10.37°, 12.72°, 14.73°, 16.50°, 18.12°, 26.71°, 31.79°, and 36.27° correspond to (011), (002), (112), (022), (013), (022), (134), (235) and (400) planes respectively, are identified which could be in excellent agreement with the previous reports.[61,62] The diffraction patterns show a single-phased cubic structure with a space group of $\bar{I}43M$ and no residual peaks. In addition, the intensity of the XRD peaks of the sample suggests that ZIF-8 materials have been successfully produced with high purity through direct precipitation method.

3.2. Vibrational analysis

To identify key changes (vibrational modes, functional groups, and behavior) in ZIF-8 materials, the FTIR was used, and the obtained spectra are shown in Fig. 2. As can be seen, the first signal at 422 cm^{-1} may correspond to Zn–N stretch vibration. The bending vibrations at 693 cm^{-1} and 759 cm^{-1} were assigned to δ(C–N) and δ(C–H) respectively. In addition, at 1146 cm^{-1} a vibration of C–N
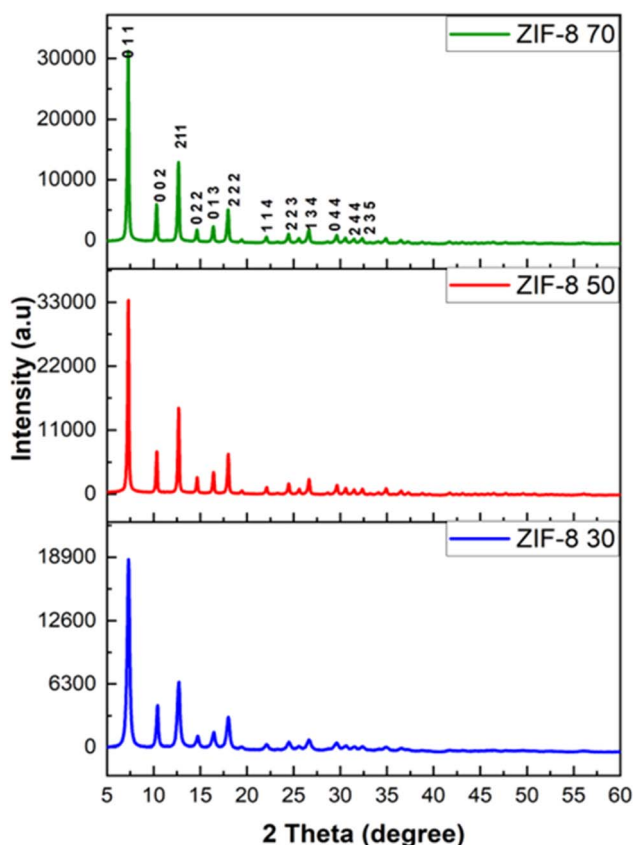

Fig. 1 XRD patterns of ZIF-8 powders synthesized at different amounts of linker: ZIF-8.30, ZIF-8.50 and ZIF-8.70.
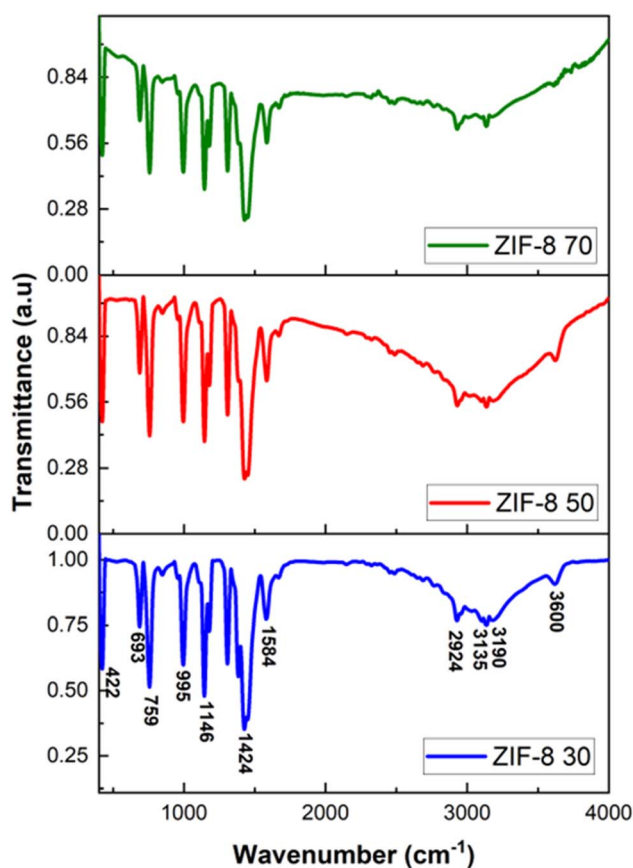

Fig. 2 FTIR spectra of the prepared ZIF-8. 30, 50 and 70 powders.

showed. Besides, stretching vibrations at 1296 cm^{-1}, 1424 cm^{-1} and 1584 cm^{-1} may be attributed to imidazole ring, ν(C=N) and C=C properly. Moreover, three peaks were observed beyond 2900 cm^{-1}: ν(C–H) aromatic stretch of 2-the ring, ν(C–H) aliphatic stretching of imidazole, ν(N–H) and ν(O–H) at 2924 cm^{-1}, 3135 cm^{-1}, 3190 cm^{-1} and 3600 cm^{-1} respectively. These peaks

were present in the FTIR spectrum of the three as-synthesized ZIF-8 materials.[63]

3.3. Morphological analysis

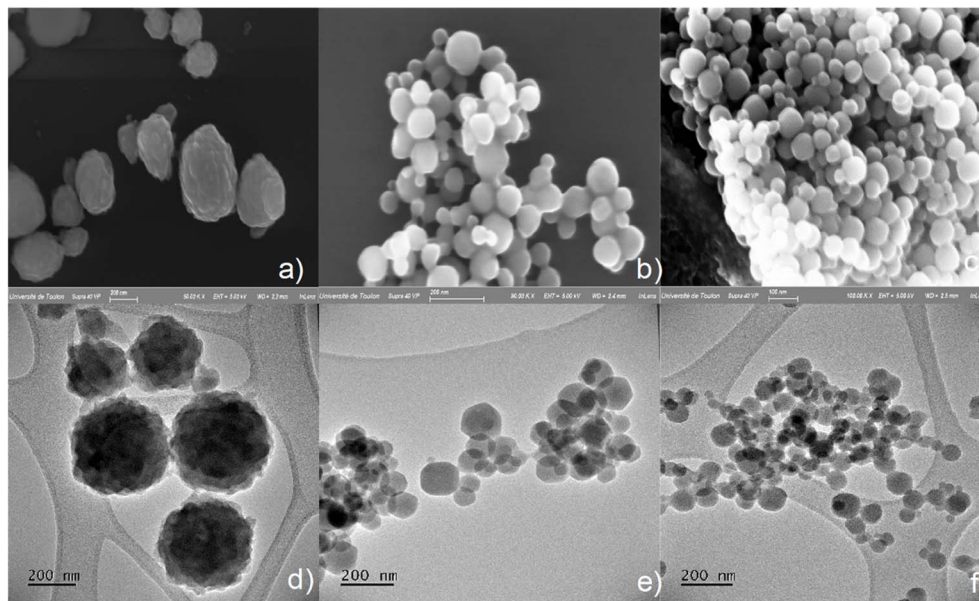Fig. 3 shows the TEM and SEM images of the samples obtained. In Fig. 3a–d, one can see the ZIF-8.30 have a spherical

Fig. 3 SEM and TEM images of ZIF-8 samples: (a and d) ZIF-8.30 (b and e) ZIF-8.50 and (c and f) ZIF-8.70.
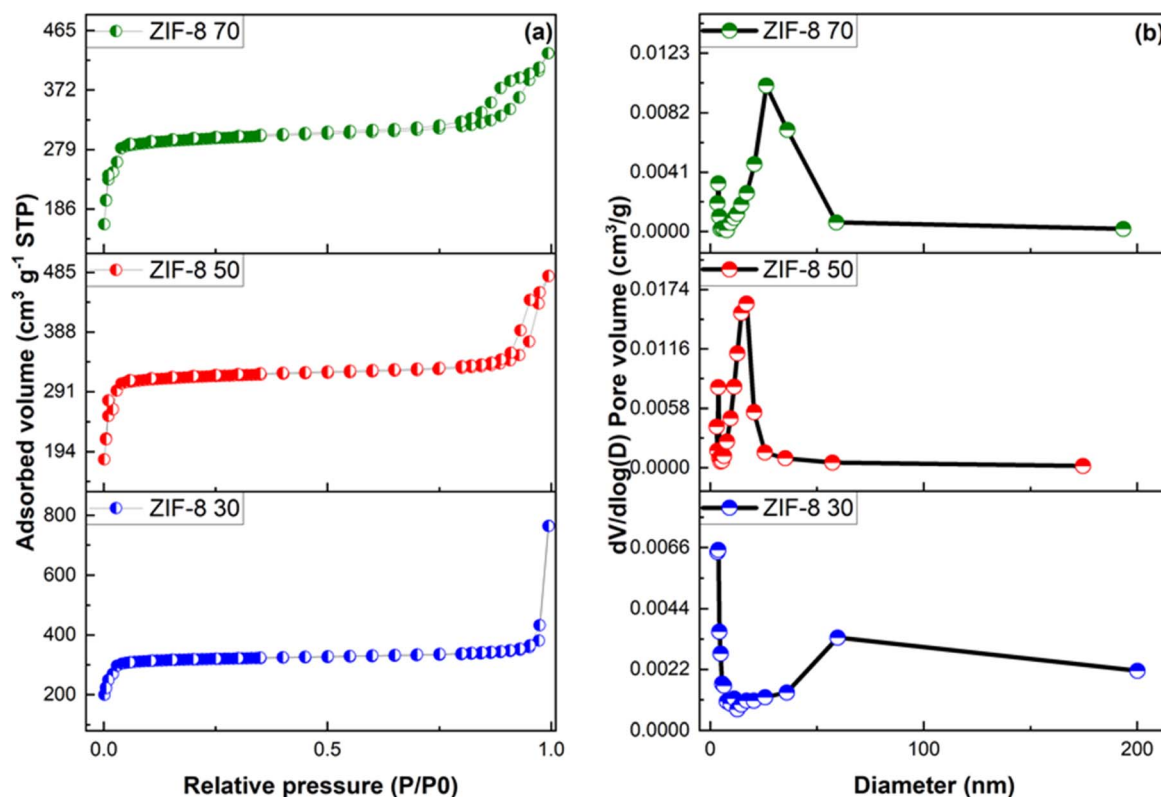

Fig. 4 (a) N$_2$ adsorption/desorption isotherms of ZIF-8 synthesized materials and (b) pore distribution of ZIF-8 materials using BJH method.

assembled of nanosheets wish is an exceptional morphology for ZIF-8 material with the size around 301 nm. The Fig. 3b, e, c and f obtained for ZIF-8.50 and ZIF-8.70 showed that ZIF-8 particles have a morphology of 3D rhombic dodecahedral (most found in the literature) ranging from 130 nm to 55 nm. The facets of ZIF-8.50 are more pronounced which can be explained by its high crystallinity, as evidenced by the fine, intense peaks of its diffractogram compared to ZIF-8.70.

3.4. Textural analysis

Fig. 4 shows the N_2 adsorption/desorption of ZIF-8 synthesized materials. According to Fig. 4(a), the isotherm plot resembled type I by International Union of Pure and Applied Chemistry (IUPAC).[64] In addition, Fig. 4(b) showed the pores size distribution for all three ZIF-8 prepared materials; the pore diameter increased from 3.8 nm, 17 nm to 26 nm, respectively for ZIF-8.30, ZIF-8.50 to ZIF-8.70; implying the major existence of micropores but also mesoporous in ZIF-8 structures. The specific surface area and micropore volume of ZIF-8 prepared materials were determined using the Brunauer–Emmett–Teller (BET) method, the specific surface were found to be 877, 948 and 1165 m^2 g^{-1} respectively for ZIF-8.30, ZIF-8.50 and ZIF-8.70.

3.5. XPS analysis

The XPS analysis conducted on the ZIF-8 samples made with different Zn : 2-methylimidazole molar ratios (1 : 30, 1 : 50, and 1 : 70) shows that all samples have similar elemental compositions and bonding environments, with some minor differences
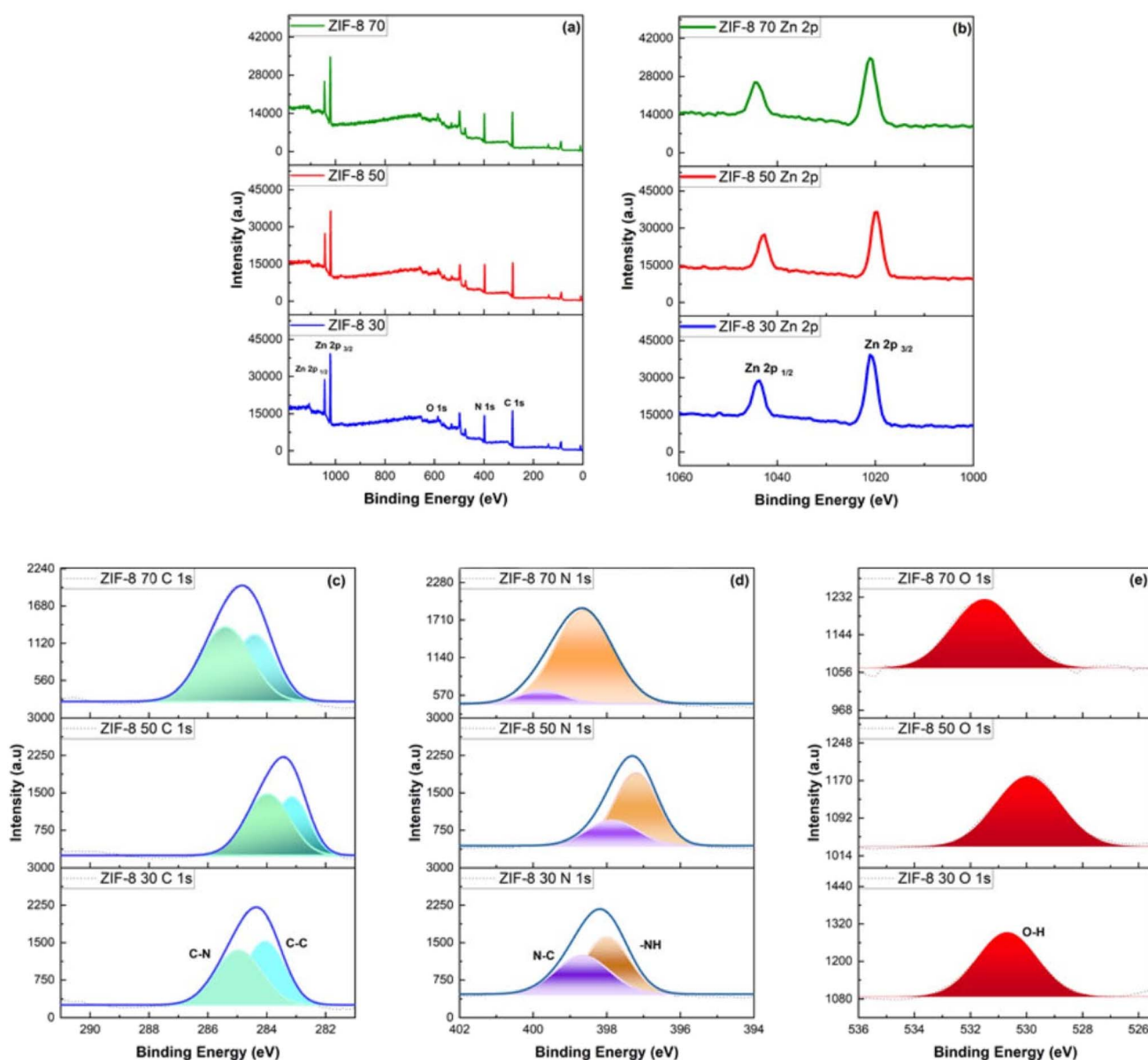

Fig. 5 (a) XPS wide scan of the prepared ZIFs (ZIF–8 70, ZIF–8 50, ZIF–8 30); (b) Zn 2p spectra ; (c) C 1s Spectra; (d) N 1s Spectra and (e) O 1s spectra off the prepared ZIFs.

(Fig. 5a). The wide-scan spectra confirm the presence of key elements such as Zn, N, C, and O (Table 2). High-resolution spectra of C 1s display clear peaks related to C–C and C–N bonding. This suggests that the organic linker framework stays intact, no matter the precursor ratio. For N 1s, the analysis reveals contributions from nitrogen atoms bonded to C(N–Zn) and a small amount of NH species, consistent with the expected imidazolate environment. There is a slight increase in the oxygen signal, mainly linked to adsorbed –OH groups around 531.7 eV, observed in the sample with a higher molar ratio (ZIF-8.70) (Fig. 5b, c, d and e). This likely results from increased porosity or surface exposure. Zn 2p spectra show the typical Zn^{2+} doublet with stable binding energies ($\sim$1021.2–1021.4 eV), confirming that the Zn-imidazolate coordination remains intact.

Notably, trace Cl signals are found in all samples, probably from leftover solvents or synthesis precursors. The quantitative data from the atomic concentration table supports these results, indicating small changes in elemental ratios that suggest variations in surface chemistry with adjustments to the molar ratio, all without affecting the overall ZIF-8 structure.[55] These findings show that increasing the 2-methylimidazole content does not harm the chemical integrity of the framework but might affect surface states and defect formation.

3.6. Optical and electrochemical characteristics

The value of the band gap energy of ZIF-8 products was considered as a determining parameter of its photocatalytic performance. The UV-visible absorption profile of ZIF-8 nanomaterials (Fig. 6a) reveals an excellent optical properties in the UV range with an absorption edge at 221,39 nm (corresponding to 5.06, 5.07 and 5.09 eV of ZIF-8.30, ZIF-8.50 and ZIF-8.70 respectively). The band gap energy (E_g) was determined using the Tauc relation $(\alpha h\nu)^{1/\gamma} = B(h\nu - E_g)$,[65] where ν denotes the photon frequency, α is the absorption coefficient, h represents Planck's constant, and γ is a parameter that depends on the nature of the band gap, taking values of 1/2 for direct transitions and 2 for indirect transitions. According to the literature, the ZIF-8 material possesses an direct bandgap.[66] In this study, the band gap energy (E_g) was obtained by extrapolating the linear region of the $(\alpha h\nu)^2$ *versus* $h\nu$ plot, yielding a value of 5.10 eV for the three prepared ZIF-8 (Fig. 6b). This energy value is approximately the same as that obtained in other studies.[59,67,68]

For n-type semiconductors, the conduction band (CB) edge is typically estimated as being about 0.2 V more negative than the flat band potential E_{fb}.[69] Therefore, based on the DRS spectral results and the calculated band gap energy, the band structure of the ZIF-8 photocatalyst can be established using the following equations $E_{CB} = V_{fb} - 0.2$ V and $E_g = E_{VB} - E_{CB}$.

A broad set of characterization techniques provided a comprehensive understanding of the structure and properties of the synthesized ZIF-8 materials. X-ray diffraction (XRD) confirmed the crystallinity and the cubic structure of ZIF-8. BET surface area analysis revealed high specific surface areas and pore size distributions, essential for adsorption capacity. SEM and TEM imaging showed the morphological evolution with varying Zn : 2-Hmim ratios, from spherical assemblies to rhombic dodecahedra. FTIR spectroscopy identified the characteristic vibrational modes of Zn–N coordination and imidazolate linkages. XPS analysis offered detailed information on the chemical environment of Zn, N, C, and O atoms as well as surface functional groups. Finally, UV-vis absorption and Tauc's plots allowed the determination of the optical band gap, which is directly relevant to the photocatalytic potential of the materials.

The main strength of this section lies in the complementarity of these techniques, which together establish strong structure–property correlations and highlight how the linker ratio affects morphology, surface chemistry, and optical properties. The limitation, however, is that these analyses remain essentially descriptive and cannot, by themselves, demonstrate adsorption or photocatalytic efficiency, which requires further functional validation.
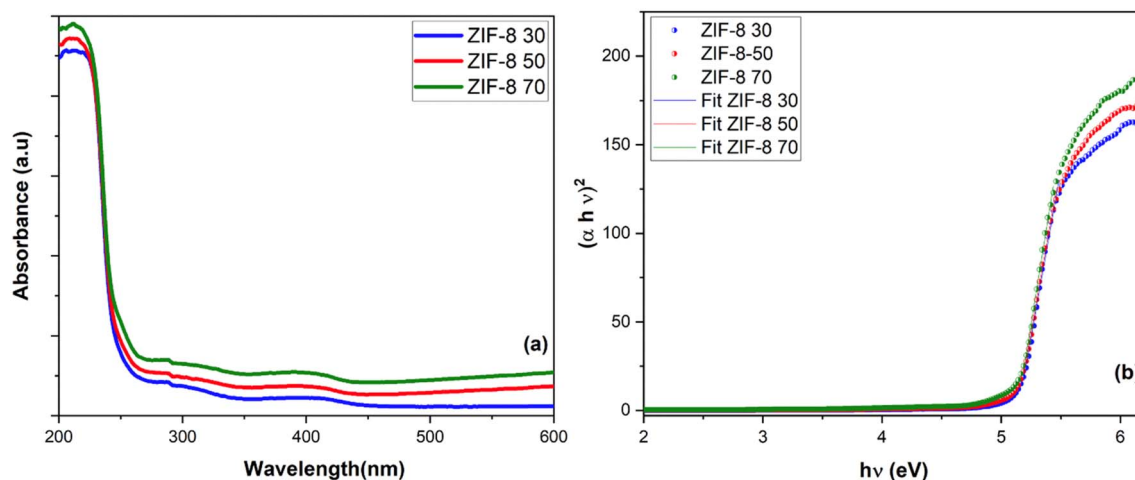

Fig. 6 (a) Absorption spectrum, (b) and Tauc's spectrum of ZIF-8 powders.

4 Evaluation of RhB adsorption using prepared of ZIF–8 materials

4.1. Optimization conditions using RSM-BBD

The influence of five independent variables on RhB adsorption efficiency was examined, namely pollutant concentration (A), 2-Hmim amount (B), pH (C), contact time (D), and catalyst dosage (E). In total, 44 experimental runs were conducted to evaluate the effect of these parameters on RhB removal (%) following the photocatalytic degradation tests. The data, analyzed with Nemrodw software and based on the Box–Behnken design (Table S2), were fitted to a quadratic model, expressed by eqn (6):

$$\begin{aligned} \text{Adsorption efficiency of RhB (\%)} = {}& 84.47 - 6.51A + 13.78B \\ & + 0.28C - 1.01D + 6.71E \\ & + 1.21A^2 - 8.37B^2 - 0.58C^2 \\ & - 3.75D^2 - 3.65E^2 \\ & + 2.37AB + 0.51AC \\ & - 2.58BC - 1.10AD \\ & + 2.68BD - 0.52CD \\ & + 3.34AE - 0.88BE \\ & + 0.28CE + 2.93DE \end{aligned} \quad (6)$$

The model terms presented in eqn (6) were selected through the use of P-value analysis (terms with a P-value < 0.05).[70] The outcomes (Table S3) demonstrate that the developed quadratic model is statistically significant with a P-value <0.05. Parameters such as pollutant concentration, 2-HmIM dosage, pH, contact time, and catalyst loading, all with $P < 0.05$, were found to exert a notable influence on RhB adsorption. Furthermore, the significance of interaction terms between variables was also evaluated based on their corresponding P-values. The sign of each regression coefficient reflects the nature of its effect: a positive value indicates that increasing the factor enhances adsorption efficiency, whereas a negative value suggests that reducing the factor promotes dye uptake. The most significant parameters positively influencing RhB adsorption, as shown in Table S3, are the linear terms B (2-HmIM), C (pH value), D

(irradiation time), E (catalyst weight), and the mutual interactions AB, AC, BD, AE, CE and DE.

Conversely, the negative coefficients of the linear term (A), the quadratic terms (A^2, B^2, C^2, D^2 and E^2), as well as the interaction terms (BC, AD, CD, and BE), indicate that these factors exert a detrimental influence on the response, leading to a reduction in adsorption efficiency. The adequacy of the model fit was evaluated using the determination coefficients (R^2 and adjusted R^2), while analysis of variance (ANOVA) was employed to assess the accuracy and statistical relevance of the proposed model. The close agreement between the adjusted R^2 (0.857) and R^2 (0.923) confirms the reliability of the model and demonstrates strong consistency between experimental and predicted values.

This indicates that the quadratic polynomial design provides a meaningful description of the relationship between the response and the process variables.[71] The regression model was further visualized through 2D contour and 3D response surface plots (Fig. 7) for RhB adsorption. These graphical representations highlight the significance of binary interactions among the investigated parameters: pollutant dose (A: X_1), HmIM amount (B: X_2), pH (C: X_3), contact time (D: X_4), and catalyst loading (E: X_5). In each case, the response was evaluated as a function of two variables while the remaining three were held constant. As shown in Fig. 7a and b, the interaction between pollutant concentration and 2-HmIM dosage (AD, X_1X_2), under optimized conditions of 70 mg catalyst, pH 7-, and 60 min contact time, was identified as the most influential factor for maximizing RhB removal efficiency. Moreover, increasing the pH value (Fig. 7c and d) produced a moderate improvement in adsorption, an effect primarily attributed to modifications in the surface charge of both the dye and the catalyst. The influence of catalyst mass on degradation efficiency is also evident (Fig. 7c, g and i), where a higher catalyst dosage enhanced RhB removal due to the increased surface area and the larger number of active sites available for adsorption. According to these graphs, the predicted value of optimal RhB removal is (90.12 ± 0.01)% with the employment of ZIF-8.70, 70 mg of
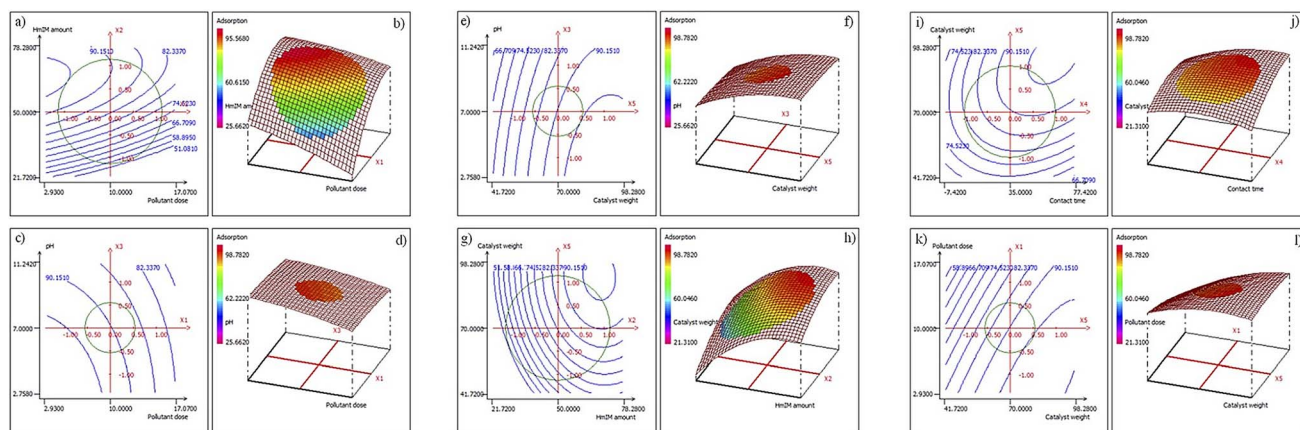

Fig. 7 2D and 3D surface response plots for RhB adsorption efficiency on ZIF-8 materials. (a and b) Effect of HmIM amount and RhB concentration. (c and d) Effect of pH and pollutant dose. (e and f) Effect of pH and catalyst weight. (g and h) Effect of catalyst weight and HmIM amount. (i and j) Effect of catalyst weight and contact time. (k and l) Effect of pollutant dose and catalyst weight.

Table 1 Predicted and experimental adsorption efficiency% of Rh-B using ZIF-8.70

Factor	Predicted adsorption (%)	Experimental adsorption (%)
Initial concentration = 10 mg L^{-1}, 2-HmIM amount = 70 mmol pH = 7, contact time = 60 min, catalyst weight = 70 mg	88	91

catalyst (ZIF-8), a pH of 7, a [RhB] concentration of 10 ppm and a contact time of 60 min. As the amount of HmIM was among the RSM parameters, ZIF-8 70 was the material which presented the highest adsorption percentage (89%) compared to the other two which can be explained by its large specific surface area of 1290 cm^2 g^{-1} and the pore diameter around 37 nm.

The experiment performed under these optimized conditions (Table 1) achieved a RhB removal efficiency of 88%, which closely matched the predicted value of 91%. These findings confirm the effectiveness of the RSM–BBD approach in delivering high adsorption performance for RhB across different scenarios generated by the software.

4.2. Experimental kinetics studies

To elucidate the adsorption mechanisms and rates (Fig. 8a), kinetic studies were conducted by investigating the uptake of contaminants as a function of contact time. Optimal experimental conditions were established at a solution pH of 7, a dosage of 0.0007 g L^{-1}, and initial concentrations of 10 mg L^{-1} for RhB. Two kinetic models were employed to describe the adsorption process: pseudo-first-order, pseudo-second-order. To deeply explain the control mechanism of the adsorption process of RhB onto ZIF-8.70, the mass transfer, chemical reaction kinetics, as well as pseudo-first-order and pseudo-second-order models were applied to interpret the adsorption process (Fig. 8b and c). The experimental results and their corresponding linearized forms are expressed by eqn (7) and (8):

$$\ln(q_e - q_t) = \ln \quad q_e - K_1 t \tag{7}$$

$$\frac{t}{q_t} = \frac{1}{K_2 q_e^2} + \frac{t}{q_e} \tag{8}$$

where q_e (mg g^{-1}) represents the adsorption capacity of the metal ion at equilibrium, q_t (mg g^{-1}) is the adsorption capacity

at time t K_1 (min^{-1}) denotes the rate constant of the pseudo-first-order kinetic model, and K_2 (g mg^{-1} min^{-1}) corresponds to the rate constant of the pseudo-second-order model.

The selection of the most suitable model was determined through a statistical error analysis, primarily using the coefficient of correlation (R^2). A higher R^2 value indicates a better fit between the model and experimental data. The resulting kinetic parameters are summarized in Table 2.

4.3. Adsorption isotherms

Adsorption isotherms provide valuable insights into the interaction mechanisms between adsorbents and adsorbates once equilibrium is reached. These models often provide insights into the distribution of active adsorption sites on the surface of the adsorbent and help clarify the underlying adsorption mechanism. As an initial step, adsorption experiments were conducted by varying the starting RhB concentration between 10 and 200 mg L^{-1} to examine its effect on adsorption efficiency and to better understand the uptake behavior. Throughout these experiments, a consistent contact time of 60 minutes and an adsorbent content of 70 mg were employed.

Out of the different adsorption isotherms, the Langmuir and Freundlich isotherms are the most used to describe the adsorption of organic and inorganic pollutants. Thus, in this part of the study, Langmuir and Freundlich isotherms were used to describe the interactions between RhB and ZIF-8.70 surface during the adsorption process. The Langmuir adsorption model is predicated on the assumption that adsorption reaches a maximum when the adsorbent surface is completely saturated with a single layer of solute molecules. The Langmuir model expressed as a linear equation is given below in eqn (9):

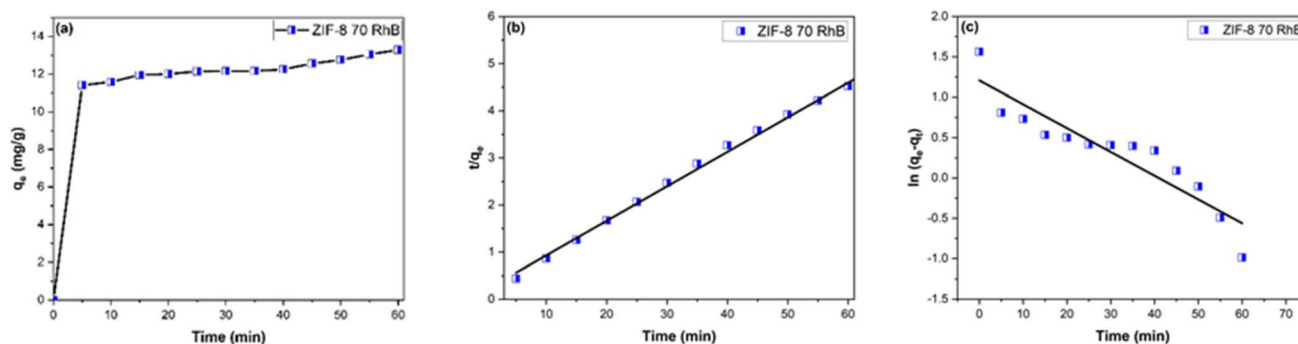$$\frac{c_e}{q_e} = \frac{1}{q_m k_L} + \frac{c_e}{q_m} \tag{9}$$

Fig. 8 (a) Effect of contact time on the RhB adsorption capacity (mg g^{-1}), (b) pseudo-second-order and (c) pseudo-first-order kinetic.

Table 2 Kinetics parameters for RhB adsorption onto ZIF–8.70

Pollutant	Pseudo first order			Pseudo second order		
	q_e (mg g^{-1})	K_1 (1/min)	R^2	q_e (mg g^{-1})	K_2 (g mg^{-1} min^{-1})	R^2
Rh-B	2.32	0.0263	0.823	13.64	0.0272	0.995

where C_e (mg L^{-1}) denotes the equilibrium concentration of the metal ion in solution, q_e (mg g^{-1}) represents the adsorption capacity at equilibrium, q_m (mg g^{-1}) corresponds to the maximum monolayer adsorption capacity of the sorbent, and K_L (L mg^{-1}) is the Langmuir constant associated with the affinity of the binding sites.

The Freundlich model accommodates heterogeneous adsorption, which involves multiple adsorption sites. Its linear form is expressed as follows:

$$\ln(q_e) = \ln(K_F) + \frac{1}{n}\ln C_e \tag{10}$$

According to the data reported in Table 3 based on the evaluated correlation coefficients (R^2), the adsorption of Rh-B fits the Langmuir isotherm model better than the Freundlich isotherm model: 0.97 compared with 0.91. This suggests that the adsorption of Rh-B onto ZIF-8.70 primarily occurs as a monolayer process occurring on a homogeneous surface. The linear plot of the Langmuir model for the adsorption of Rh-B onto ZIF-8 70 is given in Fig. 9.

Table 3 Isotherm parameters for RhB adsorption onto ZIF–8.70

Isotherm	Parameters	Rhodamine B
Langmuir	q_{max} (mg g^{-1})	91.74
	K_L (1/min)	0.1745
	R^2	0.9710
Freundlich	K_F (mg g^{-1})	17.49
	$1/n$	0.4208
	R^2	0.9039

Comparing ZIF-8.70's adsorption capacity with that of other reported adsorbents provides valuable information about its performance relative to other materials. By examining Table S4, we can see that ZIF-8.70 exhibits a competitive adsorption capacity for Rh-B compared to many other adsorbents.

4.4. Proposed mechanism

The adsorption of rhodamine B (Rh-B) onto ZIF-8.70 is a complex process influenced by a combination of electrostatic interactions, π–π stacking, and hydrogen bonding (see Fig. 10). In basic conditions, electrostatic attraction between the positively charged metallic nodes of ZIF-8.70 and the zwitterionic form of Rh-B plays a significant role. Furthermore, the aromatic nature of both Rh-B and the imidazole rings in ZIF-8.70 facilitates π–π stacking interactions.

ZIF-8.70 exhibits superior adsorption properties compared to ZIF-8.30 and ZIF-8.50 due to its higher surface area (1165 vs. 877 m^2 g^{-1}), broader pore size distribution (up to 26 nm), and smaller rhombic-dodecahedral crystals (∼55–130 nm), which shorten diffusion paths and expose more active sites. XPS analysis also reveals a greater number of surfaces –OH groups in ZIF-8.70, enhancing electrostatic and hydrogen-bonding interactions with RhB. In addition, the pH range studies (from 4 to 10) confirmed that adsorption is maximized under basic conditions, where ZIF-8 remains stable and RhB mainly exists in its zwitterionic form, favoring strong electrostatic attraction and pore accessibility. By contrast, at acidic pH RhB becomes predominantly cationic and ZIF-8 is more prone to hydrolysis, both of these factors reduce uptake. Together, these factors explain the superior adsorption capacity of ZIF-8.70.
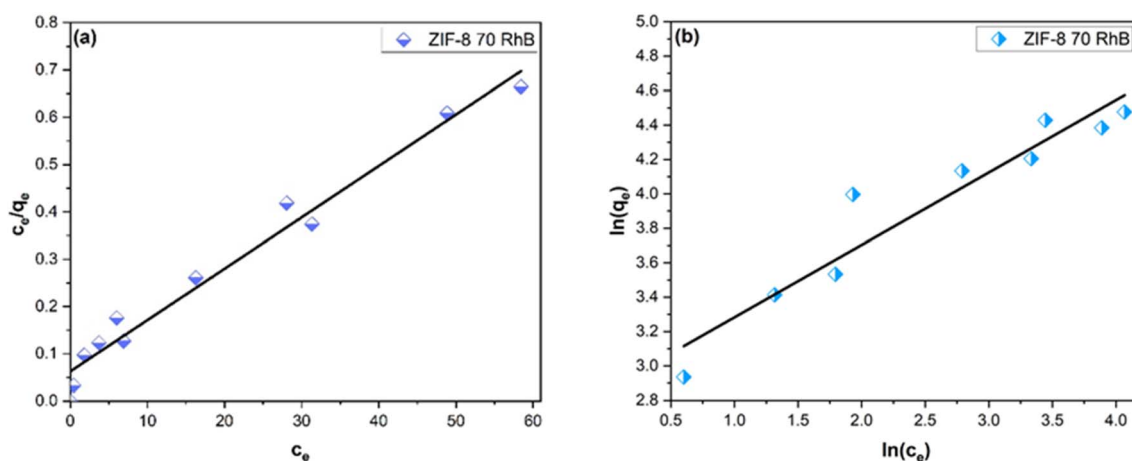

Fig. 9 (a) Linear fitting plots of Langmuir and (b) Freundlich isotherms.
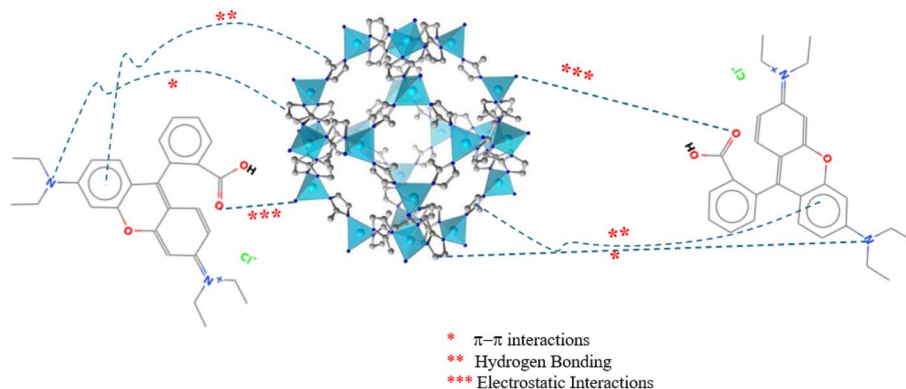
Fig. 10 Suggested mechanism of rhodamine B adsorption onto ZIF-8.70.

4.5. Reusability of ZIF-8.70 as adsorbent

Beyond its high adsorption capacity and rapid adsorption rate, the synthesis cost and recyclability of adsorbents are key factors
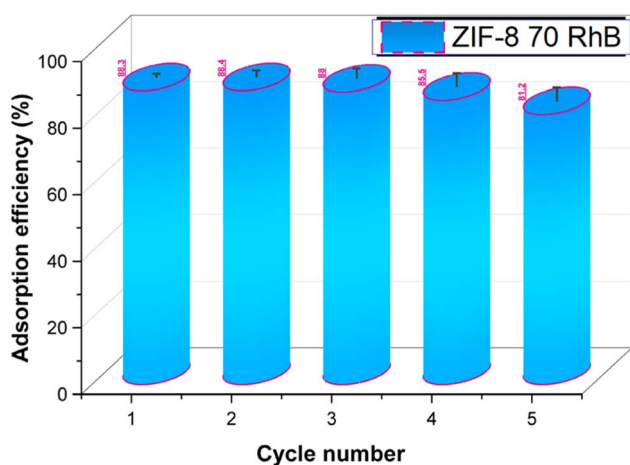

Fig. 11 Effect of recovery cycles on the removal efficiency of Rh-B onto ZIF-8.70.

for industrial applications. ZIF-8.70 was regenerated using a simple and inexpensive ethanol-washing method. After use, the material was washed, dried, and reused for subsequent adsorption cycles. Ethanol is preferred over water for regenerating ZIF-8 because it prevents hydrolysis of Zn–N bonds, thereby preserving the framework stability. Its lower surface tension and faster evaporation allow efficient pore cleaning and drying, while also dissolving and removing organic pollutants more effectively than water. This ensures that ZIF-8 maintains its crystallinity, porosity, and adsorption performance during repeated regeneration cycles.

As shown in Fig. 11, regenerated ZIF-8.70 effectively adsorb Rh-B. The material was recycled five times with minimal loss in adsorption efficiency compared to the original material. Even after five cycles, the removal capacity decreased by only 7%. Moreover, there was no significant weight loss, indicating the economic viability of ZIF-8.70 for repeated use.

The synthesis strategy presented in Section 2 demonstrated a simple, rapid, and eco-friendly approach, enabling the preparation of ZIF-8 nanomaterials at room temperature within 30 minutes without the need for surfactants. While this method offers practicality and sustainability, it provides less control
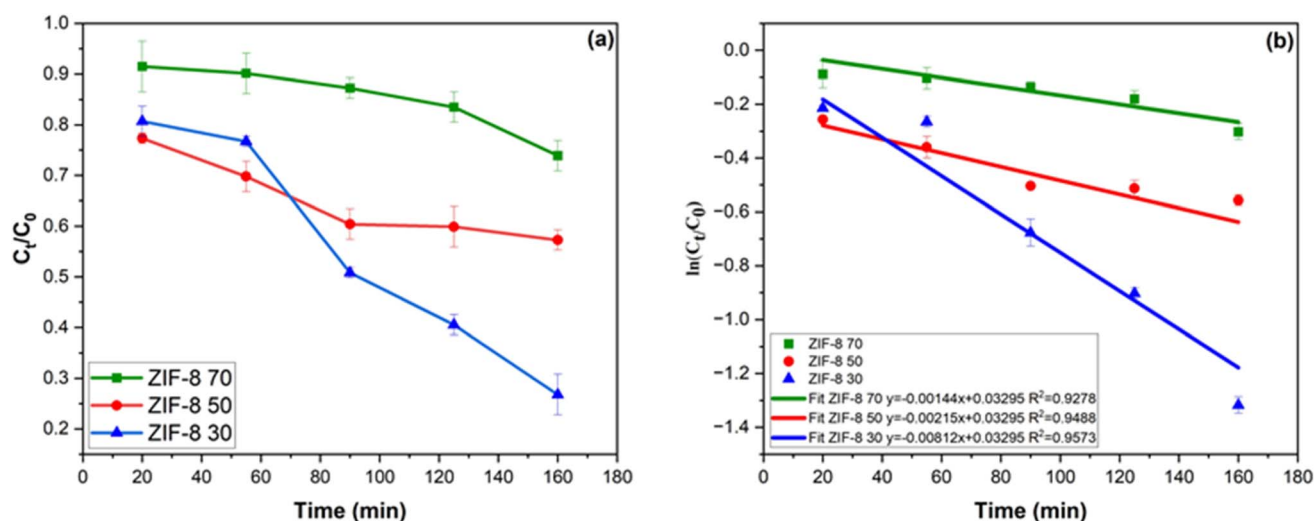

Fig. 12 (a) Variation of C_t/C_0 with illumination time for RhB degradation, (b) pseudo-first-order kinetic plot of the photodegradation process.

over uniform crystal morphology at lower Zn : 2-Hmim ratios. Section 3 focused on the structural and physicochemical characterization of the materials, confirming the successful formation of crystalline ZIF-8 and showing how different linker ratios influenced morphology, porosity, and surface chemistry. These analyses were essential for understanding material properties but remained descriptive and did not directly prove adsorption performance. Section 4 validated the functional performance of the materials, showing that ZIF-8 (1 : 70) achieved the highest adsorption capacity (91.7 mg g^{-1}) and ~91% RhB removal, with adsorption following a Langmuir isotherm and a pseudo-second-order kinetic model. The use of RSM-BBD was a major strength, allowing the optimization of key factors with strong predictive accuracy ($R^2 = 0.923$) while minimizing experimental runs. The advantage lies in combining experimental results with statistical modelling, providing reliable insights into adsorption mechanisms and optimization. However, the study was limited to testing only rhodamine B on the surface under investigation, which may not fully represent real wastewater systems.

5 Photocatalytic activity of ZIF materials

The photocatalytic performance of ZIF-8 materials has been investigated by quantifying the rate of decomposition *versus* illumination time of an aqueous solution of RhB (10 ppm) using the optimized conditions of RSM-BBD. The suspension was kept under stirring in the dark for 1 h to achieve adsorption and desorption equilibrium. Photodegradation was then monitored by recording the absorbance intensity at 554 nm, the characteristic peak of rhodamine B. At low concentrations, absorbance and concentration are directly related according to the Beer–Lambert law. The photocatalytic degradation efficiency was determined from the ratio C_t/C_0, where C_0 and C_t represent the

RhB concentrations at $t = 0$ and at time t, respectively. The reaction kinetics of the photocatalytic process are expressed by the following eqn (11):

$$\ln \frac{C_t}{C_0} = -K_{obs}\, t \qquad (11)$$

In the previous relationship, the kinetic constant was used to describe a first-order kinetic model (Langmuir Hinshelwood model). After 160 min of light exposure, the value of photocatalytic efficacy (C_t/C_0) is shown in Fig. 12a. The high performance of the three materials may be due to their specific morphology, such as their large surface area compared to that of bulk ZIF-8 materials. This extensive surface area offers abundant active sites, thereby optimizing photocatalytic processes. In addition, spherical and rhombic dodecahedral morphologies of the three ZIF-8 materials provide efficient light absorption *via* their exposed surfaces. This feature enables efficient light absorption, thereby boosting photocatalytic activity.

Furthermore, Fig. 12b illustrates photocatalytic activity, showing a linear correlation between $\ln(C_t/C_0)$ and illumination time. This relationship is defined by a rate constant of 0.00812, 0.00215 and 0.0014 min^{-1} for ZIF-8.30, ZIF-8.50 and ZIF-8.70, respectively. Consequently, the elimination efficacy was high, thanks to the electrostatic attraction forces between the cationic dye and the ZIF-8 catalysts materials.

To identify the primary oxidizing agents involved in dye degradation, radical trapping experiments were performed. L-Ascorbic acid, isopropanol, and EDTA were used as specific scavengers for $O^{2\cdot-}$, $OH^{\cdot}$, and h^+, respectively. Fig. 13a illustrates the influence of these scavengers on the photocatalytic activity of the ZIF-8 catalysts. Based on these results, it can be inferred that $O^{2\cdot-}$, $OH^{\cdot}$, and h^+ are the dominant species responsible for rhodamine B photodegradation. Upon photo-excitation, generated electron–hole pairs can react with H_2O
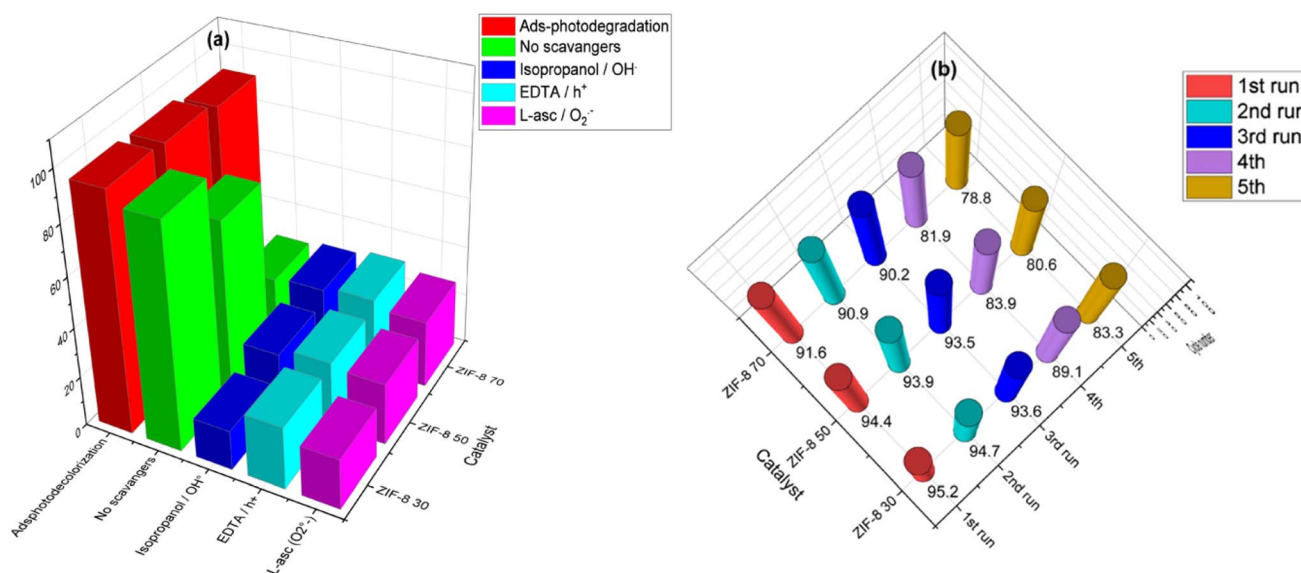

Fig. 13 (a). Elimination and photocatalytic decomposition efficiency of rhodamine B using ZIF-8 materials in the presence of a range of trappers. (b) Photocatalyst recycling test.

© 2025 The Author(s). Published by the Royal Society of Chemistry

molecules, OH^- ions, and dissolved oxygen to produce highly reactive radicals ($OH^{\bullet}/O_2^{\bullet-}$). These radicals subsequently oxidize the pollutant, leading to the mineralization of RhB into smaller molecules, ultimately yielding CO_2 and H_2O.

The stability of the ZIF-8 catalysts was assessed through recycling experiments. After each removal cycle, the catalyst was washed with ethanol and dried for reuse. Fig. 13b shows that after five consecutive photocatalyst recycling tests, there was only a slight reduction in rhodamine B removal efficiency was observed for ZIF-8.30, ZIF-8.50, and ZIF-8.70, with final values of 83.3%, 80.6%, and 78.8%, respectively. This minor decrease can be attributed to the gradual loss of accessible active sites during the recycling process. The corresponding detailed values of rhodamine B removal, together with the calculated standard deviations, are summarized in Table S5 (1 and 2).

5.1. Possible photocatalytic mechanism

Based on the M–S plots (Fig. 14), the E_{fb} of ZIF-8.30, ZIF-8.50 and ZIF-8.70 are -1.37, -1.55 and -1.53 V (vs. Ag/AgCl, pH =

Fig. 14 M–S plots of ZIF-8 30, ZIF-8 50 and ZIF-8 70.

5.6), corresponding to -0.85, -1.03 and -1.01 V (vs. RHE, pH = 5.6), respectively. Typically, the CB potential of an n-type semiconductor is about 0.2 V greater than that of the E_{fb}. Thus, the ECB of ZIF-8.30, ZIF-8.50 and ZIF-8.70 are -1.05, -1.23 and -1.21 V (vs. RHE, pH = 5.6). As shown in Fig. 6(a and b) the VBs of ZIF-8.30, ZIF-8.50 and ZIF-8.70 were therefore determined to be 4.00, 3.85 and 3.87 V, respectively.

Photoluminescence (PL) analysis was performed to evaluate the recombination behavior of electron hole pairs in the synthesized catalysts. As shown in Fig. 15a, ZIF-8 exhibited a band-edge emission at 375 nm. A notable reduction in emission intensity was observed for the ZIF-8.50 and ZIF-8.30 samples, with an even greater decrease in ZIF-8.70. This trend indicates suppressed electron recombination at oxygen vacancies, implying more efficient separation and interfacial transfer of photogenerated charge carriers. In addition, time-resolved photoluminescence (TRPL) spectra were recorded to further assess carrier lifetimes and charge separation dynamics. As shown in Fig. 15b, the fluorescence decay curves of ZIF-8.30, ZIF-8.50, and ZIF-8.70 could be fitted with a double exponential model.[72] The calculated average lifetime for ZIF-8.70, ZIF-8.50, and ZIF-8.30 were 2.3, 2.2, and 2.86 ns, respectively. Thus, the fluorescence decay results revealed excellent photogenerated charge separation and charge carriers in the ZIF-8.30, with a higher average lifetime.

Considering the above analysis and test results, we propose the following photocatalytic mechanism for the elimination of rhodamine B over ZIF-8 materials: ZIF-8.30 ZIF-8.50 and ZIF-8.70, under UV irradiation (Fig. 16).

A comparison of ZIF-8.30 with other reported materials provides valuable information about its performance relative to other materials. As depicted in Table S6, we can see that ZIF-8.30 nanomaterials exhibit competitive adsorption-photodegradation of pollutants compared to many other state-of-the-art materials.

The photocatalysis study revealed that ZIF-8 (1 : 30), despite its lower adsorption capacity, achieved the highest combined adsorption–photodegradation efficiency, reaching ~95% RhB
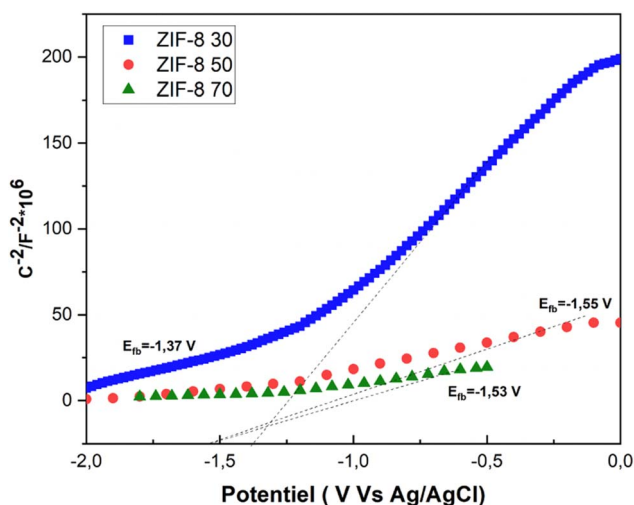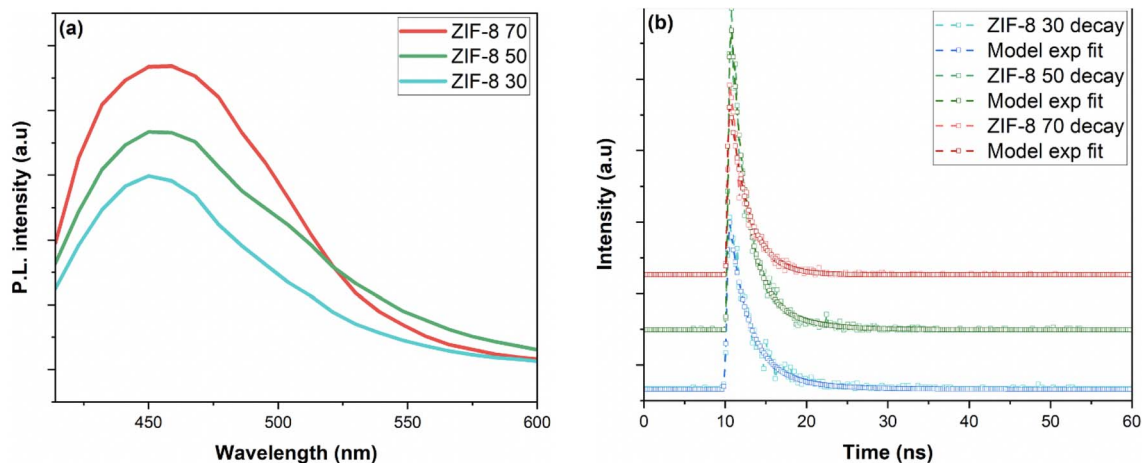

Fig. 15 (a) PL spectrum of ZIF-8 catalysts. (b) TRFL (lifetime-decay) plot of the ZIF-8 materials.
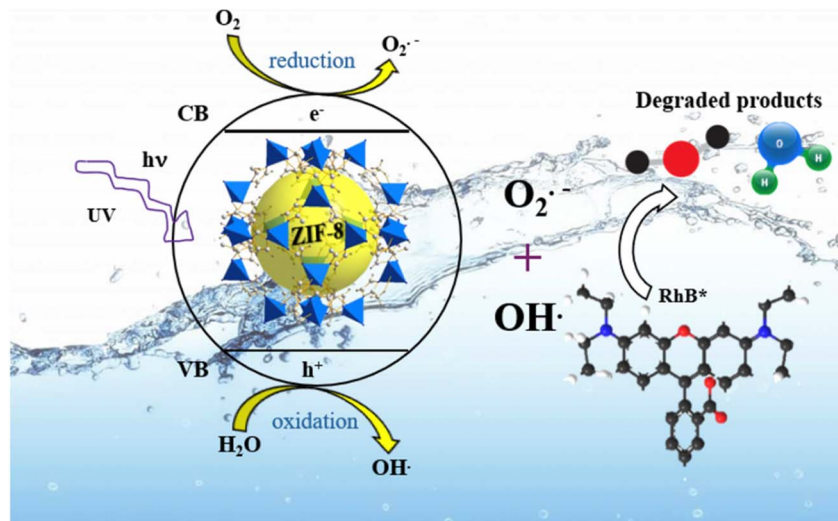
Fig. 16 Proposed mechanism for photodegradation of Rh-B using synthesized ZIF-8 materials (ZIF-8.30, ZIF-8.50 and ZIF-8.70).

removal after 160 minutes under UV light. This superior activity was linked to its unique spherical morphology, increased exposed surface, and improved charge separation, as confirmed by photoluminescence and TRPL analyses. The main advantage of this section is the demonstration of morphology-dependent photocatalytic performance and the stability of ZIF-8 materials across multiple reuse cycles. However, experiments were restricted to UV irradiation and a single dye pollutant, leaving open questions about applicability to more complex wastewater systems.

6 Conclusion

In summary, three ZIF-8 nanomaterials with distinct morphologies were successfully synthesized using a sustainable approach. X-ray diffraction patterns confirmed the formation of the expected cubic ZIF-8 structure. The ZIF-8 particles exhibited unique spherical assemblies (ZIF-8.30) and the well-known rhombic dodecahedral shape (ZIF-8.50 and ZIF-8.70). Furthermore, infrared spectroscopy revealed characteristic vibrational bands associated with the ZIF-8 phase. Analysis of variance (ANOVA) indicated the statistical significance of the quadratic model at a p-value below 0.05. The strong correlation between the adjusted R^2 and R^2 values validated the model's significance and demonstrated excellent agreement between predicted and experimental data (adjusted $R^2 = 0.857$, $R^2 = 0.923$). Under optimal conditions (pH 7, photocatalyst mass 70 mg, RhB concentration 10 ppm, irradiation time 160 min), ZIF-8 30 achieved a remarkable RhB removal efficiency of 95% with minimal adsorption. Radical trapping experiments identified superoxide, hydroxyl radicals, and holes as the primary reactive species responsible for RhB degradation. The reusability of the three ZIF-8 samples was evaluated over five consecutive cycles, demonstrating excellent stability and durability. Our study significantly advances the field of organic pollutant removal, particularly for RhB, by employing a sophisticated statistical methodology to optimize reaction parameters. This systematic approach enables the identification of optimal conditions that maximize pollutant removal efficiency, paving the way for the development of efficient and sustainable depollution technologies.

Author contributions

Conflicts of interest

There are no conflicts of interest.

Data availability

Acknowledgements

References

1 S. Affat, *Univ. Thi-Qar J. Sci.*, 2021, **8**, 130–135.

2 W. Xiao, X. Jiang, X. Liu, W. Zhou, Z. N. Garba, I. Lawan, L. Wang and Z. Yuan, *J. Cleaner Prod.*, 2021, **284**, 124773.

3 K. Tanaya, A. Kumari, A. K. Singh and D. Singh, *Water, Air, Soil Pollut.*, 2024, **235**, 516.

4 A. Tkaczyk, K. Mitrowska and A. Posyniak, *Sci. Total Environ.*, 2020, **717**, 137222.

5 S. Benkhaya, S. M. rabet and A. E. Harfi, *Inorg. Chem. Commun.*, 2020, **115**, 107891.

6 P. Abisha, C. G. Jinitha and S. Sonia, *Curr. Appl. Phys.*, 2024, **60**, 79–91.

7 U. Ahmad, S. Ullah, A. Rehman, T. Najam, S. S. Alarfaji, M. Jamshaid, O. Parkash Kumar, S. Ullah, M. Shahid, S. S. Ahmad Shah and M. Altaf Nazir, *ChemistrySelect*, 2024, **9**, e202401719.

8 S. Riaz, R. Ali, R. Iqbal, T. Najam, A. M. Al-Mohaimeed, M. S. Elshikh, M. R. Karim, S. S. A. Shah and M. A. Nazir, *ChemistrySelect*, 2025, **10**, e202500858.

9 S. Afzal, M. N. Akhtar, L. Gurbanova, M. A. El-Sheikh, A. Ahmad, C.-H. Choi, M. R. Karim, S. S. A. Shah and M. A. Nazir, *ChemistrySelect*, 2025, **10**, e02037.

10 M. A. Nazir, A. ur Rehman, T. Najam, M. F. Elsadek, M. A. Ali, I. Hossain, M. K. Tufail and S. S. A. Shah, *Catalysts*, 2024, **14**, 430.

11 A. Anum, M. A. Nazir, S. S. A. Shah, A. Y. Elnaggar, M. H. H. Mahmoud, S. M. El-Bahy, M. Malik, M. A. Wattoo and A. ur Rehman, *Fullerenes, Nanotub. Carbon Nanostruct.*, 2024, **32**, 1103–1114.

12 S. Essalmi, S. Lotfi, A. BaQais, M. Saadi, M. Arab and H. A. Ahsaine, *RSC Adv.*, 2024, **14**, 9365–9390.

13 M. Shabir, M. Yasin, M. Hussain, I. Shafiq, P. Akhter, A. S. Nizami, B. H. Jeon and Y. K. Park, *J. Ind. Eng. Chem.*, 2022, **112**, 1–19.

14 K. Adesina Adegoke, O. Samuel Agboola, J. Ogunmodede, A. Oluyomi Araoye and O. Solomon Bello, *Mater. Chem. Phys.*, 2020, **253**, 123246.

15 T. Rasheed, A. A. Hassan, M. Bilal, T. Hussain and K. Rizwan, *Chemosphere*, 2020, **259**, 127369.

16 S. Naghdi, M. M. Shahrestani, M. Zendehbad, H. Djahaniani, H. Kazemian and D. Eder, *J. Hazard. Mater.*, 2023, **442**, 130127.

17 J. Darabdhara and Md. Ahmaruzzaman, *Chemosphere*, 2022, **304**, 135261.

18 M. Beydaghdari, F. H. Saboor, A. Babapoor and M. Asgari, *ChemNanoMat*, 2022, **8**, e202100400.

19 A. Tchinsa, M. F. Hossain, T. Wang and Y. Zhou, *Chemosphere*, 2021, 284.

20 C. V. Reddy, K. R. Reddy, V. V. N. Harish, J. Shim, M. V. Shankar, N. P. Shetti and T. M. Aminabhavi, *Int. J. Hydrogen Energy*, 2020, **45**, 7656–7679.

21 Z. Lai, *Curr. Opin. Chem. Eng.*, 2018, **20**, 78–85.

22 A. Paul, I. K. Banga, S. Muthukumar and S. Prasad, *ACS Omega*, 2022, **7**, 26993–27003.

23 Y. Chen, S. Pu, D. Wang, Y. Zhang, G. Wan, Q. Zhao and Y. Sun, *J. Solid State Chem.*, 2023, **321**, 123857.

24 H. Zhao, Y. Wang and L. Zhao, *Eur. J. Inorg. Chem.*, 2017, **2017**, 4110–4116.

25 B. Bethi, G. B. Radhika, L. M. Thang, S. H. Sonawane and G. Boczkaj, *Environ. Sci. Pollut. Res.*, 2023, **30**, 25532–25545.

26 N. Liu, J. Hao, L. Chen, Y. Song and L. Wang, *Luminescence*, 2019, **34**, 193–199.

27 H. Dai, X. Yuan, L. Jiang, H. Wang, J. Zhang, J. Zhang and T. Xiong, *Coord. Chem. Rev.*, 2021, **441**, 213985.

28 Y. Song, C. Yu, D. Ma and K. Liu, *Coord. Chem. Rev.*, 2024, **499**, 215492.

29 I. Ahmad, T. Muhmood, A. Rehman, M. Zahid, M. Abohashrh, S. Nishat, Y. Raharjo, Z. Zhou and X. Yang, *J. Taiwan Inst. Chem. Eng.*, 2023, **149**, 104993.

30 S. Feng, X. Zhang, D. Shi and Z. Wang, *Front. Chem. Sci. Eng.*, 2021, **15**, 221–237.

31 Y.-R. Lee, M.-S. Jang, H.-Y. Cho, H.-J. Kwon, S. Kim and W.-S. Ahn, *Chem. Eng. J.*, 2015, **271**, 276–280.

32 K. Karuppasamy, I. Rabani, D. Vikraman, C. Bathula, J. Theerthagiri, R. Bose, C.-J. Yim, A. Kathalingam, Y.-S. Seo and H.-S. Kim, *Environ. Pollut.*, 2021, **272**, 116018.

33 F. Zafar, M. Waseem, M. Asad, A. A. Abdelwahab, M. U. Ur Rehman, N. Akhtar, A. Akhdhar and M. A. Shenashen, *Mater. Chem. Phys.*, 2023, **293**, 126985.

34 R. Wang, H. Dong, X. Li, L. Zhou, W. Zhu and T. Chen, *Chem. Eng. J.*, 2023, **478**, 147331.

35 Y. Yu, P. Li, G. Zheng, L. He, D. Ge and Z. Weng, *Microchem. J.*, 2024, **201**, 110565.

36 J. Dai, T. Chen, Q. Chen, H. Ma, X. Xu, W. Yuan and L. Wang, *Int. J. Biol. Macromol.*, 2023, **242**, 124672.

37 N. A. Mazlan, F. S. Butt, A. Lewis, R. Krishnamoorthi, S. Chen, N. Radacsi and Y. Huang, *Sep. Purif. Technol.*, 2024, **334**, 126005.

38 Q. Tong, T. Cai, J. Yuan and D. He, *J. Environ. Chem. Eng.*, 2023, **11**, 111311.

39 A. A. El Hassani, K. Tanji, I. El Mrabet, Y. Fahoul, A. El Gaidoumi, A. T. Benjelloun, M. Sfaira, H. Zaitan and A. Kherbeche, *Surf. Interfaces*, 2023, **36**, 102647.

40 B. Bouider and K. Rida, *Mater. Sci. Eng., B*, 2024, **307**, 117502.

41 K. Kuśmierek, J. Fronczyk and A. Świątkowski, *Water, Air, Soil Pollut.*, 2023, **234**, 531.

42 S. Zghal, I. Jedidi, M. Cretin, S. Cerneaux and M. Abdelmouleh, *Materials*, 2023, **16**, 1015.

43 P. Li, T. Zhao, Z. Zhao, H. Tang, W. Feng and Z. Zhang, *ACS Omega*, 2023, **8**, 4813–4825.

44 Z. M. Şenol, N. E. Messaoudi, Y. Fernine and Z. S. Keskin, *Biomass Convers. Biorefin.*, 2024, **14**, 17927–17940.

45 K. R. S. Devi, K. Karthik, J. Mackolil, B. Mahanthesh, B. S. Reghunath and D. Pinheiro, *Appl. Nanosci.*, 2023, **13**, 3749–3765.

46 A. Dabagh, M. Abali, A. Ait Ichou, R. Benhiti, F. Sinan and M. Zerbet, *J. Dispersion Sci. Technol.*, 2023, **44**, 2429–2438.

47 J. G. Vijayan, T. N. Prabhu and N. Asthana, *J. Inorg. Organomet. Polym. Mater.*, 2023, **33**, 3716–3731.

48 M. Lal, P. Sharma, L. Singh and C. Ram, *Results Eng.*, 2023, **17**, 100890.

49 M. E. S. Pedebos, D. M. Druzian, L. R. Oviedo, Y. P. M. Ruiz, A. Galembeck, G. Pavoski, D. C. R. Espinosa and W. L. da Silva, *J. Photochem. Photobiol., A*, 2024, **449**, 115404.

50 S. A. Mousavi, B. Kamarehie, A. Almasi, M. Darvishmotevalli, M. Salari, M. Moradnia, F. Azimi, M. Ghaderpoori, Z. Neyazi and M. A. Karami, *Biomass Convers. Biorefin.*, 2023, **13**, 7927–7936.

51 J. Yang, Q. Wei, D. Li, J. Yu and Z. Cai, *J. Indian Chem. Soc.*, 2023, **100**, 100958.

52 J. G. Vijayan, T. Niranjana Prabhu, A. G. Jineesh, K. Pal and S. Chakroborty, *Eur. Phys. J. E*, 2023, **46**, 23.

53 M. El Ouardi, V. Madigou, V. Chevallier, A. Merlen, A. BaQais, M. Saadi, H. Ait Ahsaine and M. Arab, *J. Environ. Chem. Eng.*, 2024, **12**, 113505.

54 A. Naboulsi, I. Naboulsi, A. Regti, M. El Himri and M. El Haddad, *Microchem. J.*, 2023, **191**, 108790.

55 J. Zheng, A. Sharma, T. Kumeria, Y. Chi, M. B. Ghasemian, G. Mao, J. Tang, P. Kumar, Md. A. Rahim and K. Kalantar-Zadeh, *Adv. Funct. Mater.*, 2024, **34**, 2300969.

56 T. Liu, K. Huang, Y. Yang, S. Wen, J. Zhang, S. Deng, S. Tan and L. Huang, *J. Mater. Chem. B*, 2024, **12**, 3481–3493.

57 R. Ma, Q. Li, J. Yan, Y. Tao, S. Hu, D. Liu, J. Gong and Y. Xiong, *Nano Res.*, 2023, **16**, 9618–9624.

58 Y. Pan, Y. Liu, G. Zeng, L. Zhao and Z. Lai, *Chem. Commun.*, 2011, **47**, 2071–2073.

59 X. Guo, S. He, Z. Meng, Y. Wang and Y. Peng, *RSC Adv.*, 2022, **12**, 17919–17931.

60 Q. Ding, D. Xu, J. Ding, W. Fan, X. Zhang, Y. Li and W. Shi, *J. Colloid Interface Sci.*, 2021, **603**, 120–130.

61 A. Demessence, C. Boissière, D. Grosso, P. Horcajada, C. Serre, G. Férey, G. J. Soler-Illia and C. Sanchez, *J. Mater. Chem.*, 2010, **20**, 7676–7681.

62 S. R. Venna and M. A. Carreon, *J. Am. Chem. Soc.*, 2010, **132**, 76–78.

63 C. Singh, C. B. Jha, N. Kumar, R. Singh, H. Ojha, S. Upadhyayula, R. Varshney and R. Mathur, *J. Mater. Sci.*, 2022, **57**, 18561–18577.

64 A. Moradi, M. Kalaee, O. Moradi, N. M. Mahmoodi and D. Zaarei, *J. Mol. Struct.*, 2024, **1304**, 137642.

65 Y. Feng, S. Lin, S. Huang, S. Shrestha and G. Conibeer, *J. Appl. Phys.*, 2015, **117**, 125701.

66 R. Yang, X. Yan, Y. Li, X. Zhang and J. Chen, *ACS Appl. Mater. Interfaces*, 2017, **9**, 42482–42491.

67 J. G. Vitillo and L. Gagliardi, *Chem. Mater.*, 2021, **33**, 4465–4473.

68 J. Liu, R. Li, X. Zu, X. Zhang, Y. Wang, Y. Wang and C. Fan, *Chem. Eng. J.*, 2019, **371**, 796–803.

69 Q. Liu, M. Wang, Y. He, X. Wang and W. Su, *Nanoscale*, 2018, **10**, 19100–19106.

70 T.-H. Le and S. Shin, *J. Korean Soc. Qual. Manag.*, 2018, **46**, 39–74.

71 M. A. Bezerra, R. E. Santelli, E. P. Oliveira, L. S. Villar and L. A. Escaleira, *Talanta*, 2008, **76**, 965–977.

72 G. Žerjav, J. Teržan, P. Djinović, Z. Barbieriková, T. Hajdu, V. Brezová, J. Zavašnik, J. Kovač and A. Pintar, *Catal. Today*, 2021, **361**, 165–175.